Title

Coupled thermal–hydrological–mechanical modeling of CO2-enhanced coalbed methane recovery

Authors

Ma, Tianran
Rutqvist, Jonny
Oldenburg, Curtis M
et al.

Publication Date

2017-06-01

DOI

10.1016/j.coal.2017.05.013

Peer reviewed

Coupled thermal–hydrological–mechanical modeling of CO_2-enhanced coalbed methane recovery

Tianran Ma [a, b, c], Jonny Rutqvist [c], Curtis M. Oldenburg [c], Weiqun Liu [a, b]

[a] Key Laboratory of Coal-based CO_2 Capture and Geological Storage, China University of Mining and Technology, Xuzhou, Jiangsu, China

[b] State Key Laboratory for Geomechanics and Deep Underground Engineering, China University of Mining and Technology, Xuzhou, Jiangsu, China

[c] Lawrence Berkeley National Laboratory, Energy Geosciences Division, Berkeley, CA, USA

This version was submitted for publication in International Journal of Coal Geology

Final version published in June 2017 as

Ma T., Rutqvist J., Oldenburg C.M., Liu W. Coupled thermal–hydrological–mechanical modeling of CO2-enhanced coalbed methane recovery. *International Journal of Coal Geology.* 179, 81–91 (2017). http://dx.doi.org/10.1016/j.coal.2017.05.013.

Abstract

CO_2-enhanced coalbed methane recovery, known as CO_2-ECBM, is a potential win-win approach for enhanced methane production while simultaneously sequestering injected anthropogenic CO_2 to decrease CO_2 emissions to the atmosphere. In this paper, CO_2-ECBM is simulated using a coupled thermal–hydrological–mechanical (THM) numerical model that accounts for multiphase (gas and water) flow and solubility, multicomponent (CO_2 and CH_4) diffusion and adsorption, as well as heat transfer and coal deformation. The coupled model is based on the TOUGH-FLAC simulator, applied here for the first time for modeling CO_2-ECBM. The capacity of the simulator for modeling methane production is first verified by code-to-code comparison with the general-purpose finite element solver COMSOL. Then the TOUGH-FLAC simulator is applied in an isothermal simulation to study the variations in permeability evolution during a CO_2-ECBM operation, considering four different stress-dependent permeability models implemented into the simulator. Finally, the TOUGH-FLAC simulator is applied in non-isothermal simulations to model THM responses during a CO_2-ECBM operation. The simulations show that permeability evolution, mechanical stress, and deformation are all affected by changes in pressure, temperature and adsorption swelling, with adsorption swelling having the biggest impact. The calculated stress changes did not induce any mechanical failure in the coal seam except near the injection well in one case of a very unfavorable stress field.

Keywords: Coupled THM model; CO_2 sequestration; CBM production; TOUGH-FLAC, CO_2-ECBM

Highlight:

(1) Coupled thermal–hydrological–mechanical (THM) numerical modeling of CO_2-ECBM

(2) Application of the TOUGH-FLAC simulator for CO_2-enhanced coalbed methane recovery

(3) Code-to-code comparison between TOUGH-FLAC and the finite element solver COMSOL

(4) Mechanical failure occurs near the injection well in the coal seam with an extensional *in situ* stress state

1 Introduction

Carbon dioxide (CO_2) injection into geologic formations, such as oil and gas reservoirs, saline aquifers, and coal seams, is recognized as a promising approach to reducing CO_2 emissions into the atmosphere and thereby mitigating climate change. CO_2 injection into coal seams combined with enhanced coalbed methane (CH_4) recovery (ECBM) can provide economic benefits because CH_4 production would offset some of the cost of CO_2 capture and storage (Moore, 2012; White et al., 2005). Because of the strong adsorption capacity of coal, CO_2 would displace CH_4 and adsorb onto the surface of the coal matrix, thereby improving the production of CBM.

In the process of CBM extraction and CO_2-ECBM recovery, the permeability of coal is a key parameter that varies drastically due to geomechanical effects (Liu et al., 2011; Pan and Connell, 2012; Roadifer et al., 2003). The geomechanical behavior of coal is usually thought to be affected by two components. One is associated with the effective stress changes caused by the pore-pressure variation, and the other is swelling/shrinkage strain, which is induced by CH_4 desorption or CO_2 adsorption onto the matrix skeleton. The effective compressive stress increases as the decreasing pore pressure reduces the apertures of fractures within the cleat system, which in turn reduces the absolute permeability of the coal. However, the depressurization also causes a concentration difference between the matrix and cleats, and this difference accelerates the release of CH_4. As the CH_4 desorbs from the matrix, the deformation caused by matrix shrinkage increases the cleat permeability. Added on top of pressure and adsorption swelling, thermal expansion may also impact cleat permeability if there is a marked difference between injection and formation temperatures.

Several permeability models have been developed to predict the dynamic evolution of coal permeability (Gray, 1987; Seidle et al., 1992; Palmer and Mansoori, 1998; Shi and Durucan, 2004; Cui and Bustin, 2005; Robertson and Christiansen, 2006; Liu and Rutqvist, 2009; Palmer, 2009; Wang et al., 2009; Gu and Chalaturnyk, 2010; Moore et al., 2014; Ma et al., 2016). According to the classification proposed by Gu and Chalaturnyk (2005), there are two types of permeability models that consider the effects of geomechanics: strain-based and stress-based models. In the strain-dependent models, the volumetric deformation of coal changes the porosity of the cleat system. Then, a cubic law is usually adopted between the permeability ratio and porosity ratio to describe the permeability changes. In the stress-dependent models, stress changes are influenced by geomechanical deformations and permeability is related to stress, frequently through an exponential relationship between permeability and changes in effective mean or horizontal stress. Overall, the above permeability models demonstrate the significance of permeability variations with geomechanical responses during the CBM/ECBM process.

Several of the current CBM numerical simulators, such as CMG, Eclipse, COMET 2/3 and METSIM, use analytical permeability models with simplified analytical models of geomechanical effects on permeability (Law et al., 2004). Based on the assumption that the coal reservoir is under uniaxial strain or a constant overburden stress, the permeability is described as a function of the pore pressure and swelling/shrinkage strain. These methods involve one-way coupling and only consider the geomechanical effects of coal deformation on fluid migration and heat transfer. However, no geomechanical equations are solved in the numerical simulations and thus the actual geomechanical behavior of coal is not studied. The limitations of such analytical permeability models have been discussed by Gu and Chalaturnyk (2010).

The aforementioned CBM simulators ignore the solubilities of CO_2, N_2, and CH_4, which are involved in the mass transfer between the gaseous phase and aqueous phase. The solubility, which is related to the pore pressure, temperature, and brine salinity, is a significant factor for CO_2 migration and storage in geological sequestration (Benson and Cole, 2008). Furthermore, Cui and Bustin suggested that the adsorption and solubility capacity of CH_4 and CO_2 are the two most important factors that control their transport through coal seams (Cui et al., 2004). A few simulators have been developed and applied for modeling thermal, hydrological, and mechanical (THM) behavior of coal seams. For example, Connell (2009) linked the fluid simulator SIMEDII, which considers CO_2 dissolution in water (Pan and Connell, 2011), to the FLAC3D geomechanical software to investigate the coupled HM process during CH_4 production and CO_2-ECBM (Connell and Detournay, 2009). Gu and Chalaturnyk (2005; 2006) coupled CMG, a commercial simulator of coalbed methane reservoirs, with FLAC3D to analyze thermal–hydrological–mechanical (THM) behavior during gas depletion.

In this study, the TOUGH-FLAC simulator (Rutqvist et al., 2002; Rutqvist, 2011) was adapted for modeling coupled THM processes during CO_2-ECBM. TOUGH-FLAC is based on linking the multiphase flow and heat transport simulator TOUGH2 (Pruess et al., 2012) with the geomechanical simulator FLAC3D (Itasca, 2011). The simulator TOUGH-FLAC has been widely applied in studies of CO_2 sequestration, enhanced geothermal systems, nuclear waste, hydrate-bearing sediments, and heavy oil production (Rutqvist and Tsang, 2002; Rutqvist et al., 2005; Rutqvist et al., 2012; Jeanne et al., 2014; Kashihara and Rutqvist, 2016). In this paper, TOUGH-FLAC is applied to the simulation of coalbed methane production and CO_2-ECBM for the first time. For adaptation of TOUGH-FLAC for CO_2-ECBM, a new TOUGH2 equation-of-state module based on EOS7C (Oldenburg et al., 2004) named EOS7C-ECBM (Webb, 2011) is utilized. With this module TOUGH-FLAC can simulate multiphase (gas and water) flow and gas solubility, multicomponent (CO_2 and CH_4) diffusion and adsorption, heat transfer, and mechanical deformation. First, the capacity of the simulator for modeling CH_4 production is verified by code-to-code verification with the general-purpose finite element solver COMSOL. Then the TOUGH-FLAC simulator is applied in an isothermal simulation to study the variations in permeability evolution during a CO2-ECBM operation, considering four different stress-dependent permeability models implemented into the simulator. Finally, the TOUGH-FLAC simulator is applied to model THM responses during a CO_2-ECBM operation, including CO_2 and CH_4 migration, pressure, temperature, and saturation changes, and how these changes affect mechanical deformations and stress, as well as the potential for mechanical failure in the coal seam.

2 Mathematical model

2.1 General balance equations

The general form of the mass and energy balance equations in TOUGH2 is expressed as follows (Pruess et al., 2012):

$$\frac{d}{dt}\int_{V_n} M^K \, dV_n = \int_{\Gamma_n} F^K \cdot n \, d\Gamma_n + \int_{V_n} q^K \, dV_n \tag{1}$$

where M^K is the mass or energy per unit volume, F^K is mass or heat flux, and q^K is a source or sink per unit volume. The liquid mass is described as follows:

$$M_l^K = \phi \sum_l S_l \rho_l X_l^K \tag{2}$$

where ϕ is the porosity of coal, S_l is liquid saturation, ρ_l is the liquid density and X_l^K is the mass fraction in the liquid phase. TOUGH2 assumes that there is no adsorption/desorption time lag in the model, i.e., the CH_4 adsorbed onto the matrix diffuses instantaneously into the fractures in the cleat system. Thus, the total mass of gas component consists of free gas and adsorbed gas:

$$M_g^K = \phi \sum_g S_g \rho_g X_g^K + (1-\phi)\rho_{coal} G_{si} \rho_{gs} \tag{3}$$

where ρ_{coal} is the coal density and ρ_{gs} is the gas density under standard conditions of 1 atmosphere of pressure (0.101325 MPa) and 15.56 $℃$. The gas storage capacity G_{si} is given by the extended Langmuir function as follows:

$$G_{si} = G_{sLi}\left[1-(w_a - w_{we})\right]\frac{P_g y_i / P_{Li}}{1 + P_g \sum_{i=1}^{nc} y_i / P_{Li}} \tag{4}$$

where G_{sLi} and P_{Li} are the Langmuir pressure and volume constants, respectively, of component i ; w_a is the ash weight fraction; w_{we} is the moisture weight fraction; P_g is the gas pressure; y_i is the mole fraction of component i in the gas phase; and nc is the number of components. Here, the effects of temperature on the Langmuir adsorption function are ignored. Additionally, the adsorption of water vapor is also not considered in the current model.

The mass flux F^K can be decomposed into two components: advective and diffusive fluxes:

$$\begin{aligned} F^K &\vee ¿_{dif} \\ F^K &\vee ¿_{adv} + ¿ \\ F^K &= ¿ \end{aligned} \tag{5}$$

The advective flux is calculated by Darcy's law:

$$F^K \vee ¿_{adv} = \sum_\beta X_\beta^K \left[-k \frac{k_{r\beta}}{\mu_\beta} \rho_\beta (\nabla P_\beta - \rho_\beta g) \right] \tag{6}$$
¿

The diffusive flux $F^K \vee \iota_{dif}$ can be described by Fick's Law or the Dusty gas model (Webb, 2011). In this paper, Fick's Law is chosen to describe gas diffusion.

The thermal energy term is presented as follows:

$$M^h = (1-\phi)\rho_R C_R T + \phi \sum_\beta S_\beta \rho_\beta u_\beta \tag{7}$$

where ρ_R and C_R are rock grain density and specific heat, respectively. T is the current temperature, and u_β is the internal energy of phase β. The energy flux includes conductive and convective components:

$$F^h = -\lambda \nabla T + \sum_\beta h_\beta F_\beta \tag{8}$$

where λ is thermal conductivity and h_β is specific enthalpy.

2.2 Capillary pressure function

The capillary pressure is the pressure difference between the gas pressure and liquid pressure and varies with saturation. The van Genuchten model is adopted for the simulations in this paper:

$$p_c = min\left(max\left(-p_{max}, -p_0\left[\left(S^\iota\right)^{-1/m} - 1\right]^{1-m}\right), 0\right) \tag{9}$$

$$S^\iota = \frac{S_l - S_{lr}}{S_{ls} - S_{lr}} \tag{10}$$

where m is the van Genuchten coefficient related to the pore size distribution, p_{max} is the maximum capillary pressure, S^ι is the effective liquid saturation and S_{lr} is the residual saturation in the liquid phase.

2.3 Relative permeability function

A typical relative permeability relationship adopted in the paper is plotted in Fig. 1 (Webb, 2011). In Fig. 1, k_{rw} and k_{rg} are the relative permeabilities of the gas and liquid phases, respectively. Note that several different capillary functions and relative permeability relationships are provided in TOUGH2 for different situations.

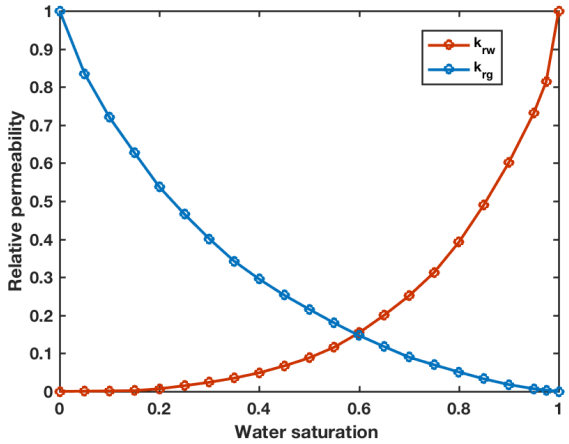

Fig. 1. Example curves of relative permeability

2.4 Geomechanical model of coal deformation

The quasi-static equation of motion can be written as follows:

$$\nabla \cdot \sigma + F = 0 \tag{11}$$

where F is the body force. Based on the constitutive relationship of poroelasticity and considering the CH_4 desorption-induced strain and thermal strain, the total stress σ is given as follows (with tensile stress being a positive quantity):

$$\sigma = \sigma' - \alpha I p = D : \varepsilon^e - \alpha I p = D : \left(\varepsilon - \varepsilon_s - \varepsilon_T\right) - \alpha I p \tag{12}$$

where σ' is the effective stress, p is the mean pore pressure, D is the tangential stiffness matrix, ε^e is elastic strain, α is Biot's coefficient and I is the unit tensor. The mean pore pressure p is calculated as follows.

$$p = S_l p_l + S_g p_g \tag{13}$$

where subscripts l and g identify the liquid and gas phases, respectively.

The infinitesimal total strain ε is calculated based on the displacement gradient.

$$\varepsilon = \frac{1}{2}\left(\nabla u + \nabla^T u\right) \tag{14}$$

Assuming isotropic shrinkage/swelling, the desorption-induced linear strain ε_s in each direction is calculated using a Langmuir-type equation:

$$\varepsilon_s = \frac{1}{3}\varepsilon_{sv} = \frac{1}{3} I \sum_{i=1}^{nc} \varepsilon_{gi} \Delta G_{si} \tag{15}$$

where ε_{sv} is desorption-induced volumetric strain and ε_{gi} is the volumetric strain coefficient.
The thermal strain is given as follows:

$$\varepsilon_T = \alpha_T I \Delta T \tag{16}$$

where α_T is the thermal linear expansion coefficient and ΔT is the temperature change from the initial value.

2.5 Stress-dependent porosity and permeability models

The following stress-dependent porosity and permeability models (Ma et al., 2016) were implemented in TOUGH-FLAC.

$$\phi_{M\wedge R} = \alpha + (\phi_0 - \alpha)\exp\left(\frac{-\Delta\sigma_m^{'}}{K}\right) \tag{17}$$

$$\frac{k_{M\wedge R}}{k_0} = \left(\frac{\phi_{M\wedge R}}{\phi_0}\right)^3 = \left[\frac{\alpha}{\phi_0} + \frac{(\phi_0 - \alpha)}{\phi_0}\exp\left(\frac{-\Delta\sigma_m^{'}}{K}\right)\right]^3 \tag{18}$$

where ϕ_0 and k_0 represent the initial porosity and permeability at initial stress, K is the bulk modulus and $\sigma_m^{'}$ is effective mean stress ($\sigma_m^{'} = \frac{\sigma_x^{'} + \sigma_y^{'} + \sigma_z^{'}}{3}$¿ .

Three additional porosity and permeability models, P&M, C&B and S&D (Palmer and Mansoori, 1998; Cui and Bustin, 2005; Shi and Durucan, 2004), were also implemented in TOUGH-FLAC (Table 1).

Table 1 Porosity and permeability models in TOUGH-FLAC

Model	Porosity	Permeability
P&M	$\phi_{P\wedge M} = \phi_0 + \frac{\alpha}{K}\Delta\sigma_m^{'}$	$\frac{k_{P\wedge M}}{k_0} = \left(1 + \frac{\alpha}{K\phi_0}\Delta\sigma_m^{'}\right)^3$
C&B	$\phi_{C\wedge B} = \phi_0\exp\left(\frac{\Delta\sigma_m^{'}}{K_p}\right)$	$\frac{k_{C\wedge B}}{k_0} = \exp\left(\frac{3\Delta\sigma_m^{'}}{K_p}\right)$
S&D	$\phi_{S\wedge D} = \phi_0\exp\left(\frac{\Delta\sigma_h^{'}}{K_p}\right)$	$\frac{k_{S\wedge D}}{k_0} = \exp\left(\frac{3\Delta\sigma_h^{'}}{K_p}\right)$

In Table 1, K_p is the pore space modulus, and $\Delta\sigma_h^{'}$ is the effective horizontal stress change.

3 TOUGH-FLAC coupling procedure

A schematic diagram of the coupling procedure between TOUGH2 and FLAC3D for ECBM is illustrated in Fig. 2. The approach follows the general coupling procedure of TOUGH2 and FLAC3D established in Rutqvist et al. (2002) and Rutqvist (2011), but is adapted here for CO_2-ECBM. The calculations of multiphase flow and solubility, multicomponent adsorption and diffusion, and thermal transfer are performed in TOUGH2 with the EOS7C-ECBM equation-of-state module (Webb, 2011) which is built on EOS7C (Oldenburg et al., 2004). At each time step, the geomechanical deformation, including effects of pore-pressure, swelling and thermal expansion is calculated in FLAC3D using a quasi-static mechanical analysis. The THM model adopts the explicit-sequential method, and the porosity and permeability are updated at the beginning of each time step.

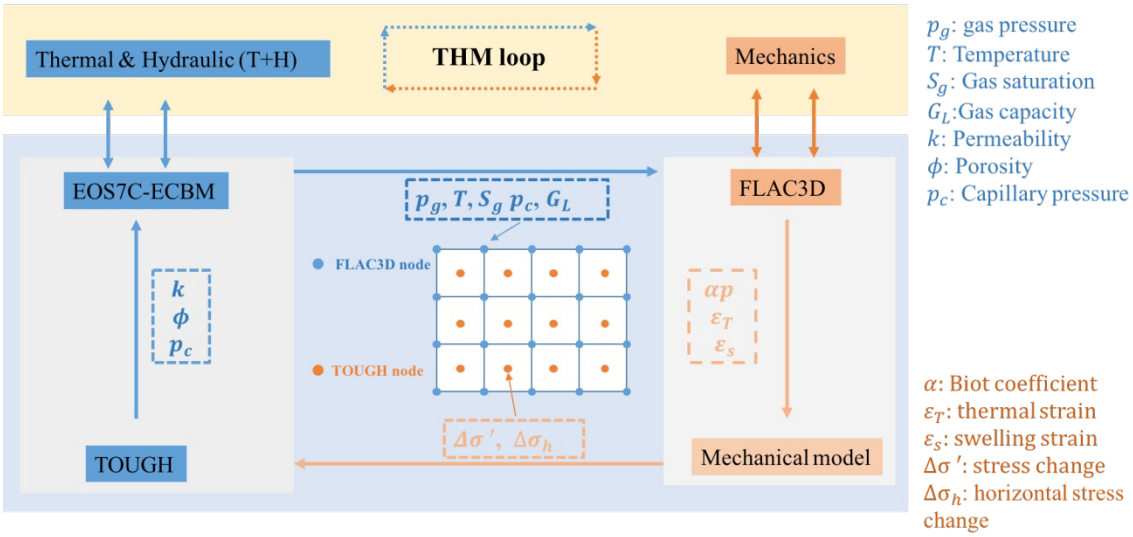

Fig. 2 Schematic diagram of coupling between TOUGH2 and FLAC3D (modified from Rutqvist (2011)).

4 Code-to-code verifications

In this section, a code-to-code verification between TOUGH2, TOUGH-FLAC, and COMSOL Multiphysics is presented for code verification modeling of CBM production. COMSOL is a commercial general purpose finite element software which has also been successfully applied to study coalbed methane production and ECBM processes (Ma et al., 2016).

The domain of the model for the code-to-code comparison is shown in Fig. 3. The model size is 500 m × 10 m × 10 m in the x-, y- and z- directions, respectively. In the case of TOUGH2 and TOUGH-FLAC, the model domain was discretized using a grid with different directional dimensions. In the case of COMSOL, a relatively fine triangular mesh was used to discretize the domain. In all the models, the local area near the production boundary was discretized with a fine mesh to improve the convergence and robustness of the numerical solution. The simulation parameters are listed in Table 2. The properties of CH_4 must be provided in COMSOL, whereas they are automatically calculated in TOUGH2 as a function of pressure and temperature as defined in the EOS7C-ECBM equation-of-state module.

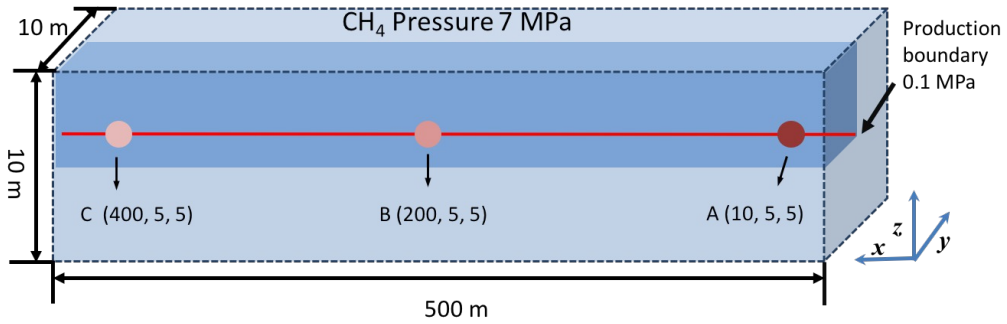

Fig. 3 Illustration of CH_4 extraction from a rectangular domain with constant pressure on the right-hand side boundary

Table 2 Parameters for CBM production

Parameters	Value
Initial porosity, ϕ_0 (%)	0.5
Initial permeability, k_0 (m^2)	5.0×10^{-15}
Young's modulus of coal, E (GPa)	3.5
Poisson's ratio of coal, ν	0.25
Density of the coal seam, ρ_c (kg/m^3)	1300
Moisture content	0.0672
Ash content	0.156
Reference density of CH_4, ρ_{ga} (kg/m^3)	0.67
Viscosity of CH_4, μ ($Pa \cdot s$)	1.3×10^{-5}
Compressive coefficient of CH_4 ($1/Pa$)	1.078×10^{-5}
Langmuir pressure constant of CH_4, p_L (kPa)	4688.5
Langmuir volume constant of CH_4, V_L (m^3/kg)	0.0152
Langmuir volumetric strain constant of CH_4, ε_L	0.01

Initially the model domain is fully saturated with coalbed methane at an initial pore pressure of 7 MPa. Methane is produced from the right boundary at a constant pressure of 0.1 MPa. No flow boundaries are applied at the other boundaries. The mechanical boundary conditions include a free surface at the top boundary and roller constraints at the other boundaries.

Fig. 4 shows the pore pressure evolution at Points A, B, and C for TOUGH2 and COMSOL in which geomechanical effects are not considered and the permeability is constant. The evolution of the pore pressure and permeability ratio at Points A, B, and C in the coupled case for TOUGH-FLAC and COMSOL are shown in Fig. 5. In this scenario, the porosity and permeability vary with the mean effective stress, as expressed in Eqs. (17) and (18).

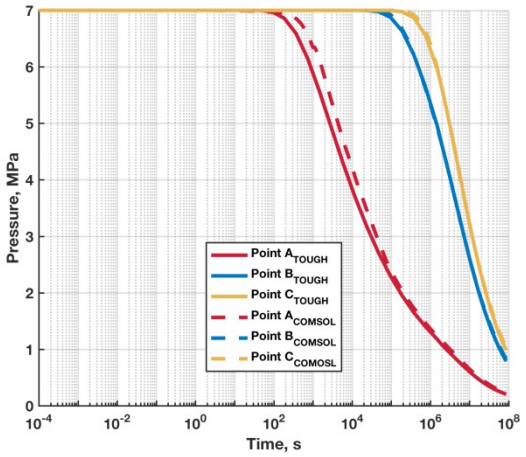

Fig. 4 The evolution of pressure during CBM production at Points A, B and C in TOUGH2 and COMSOL for uncoupled model with constant permeability.

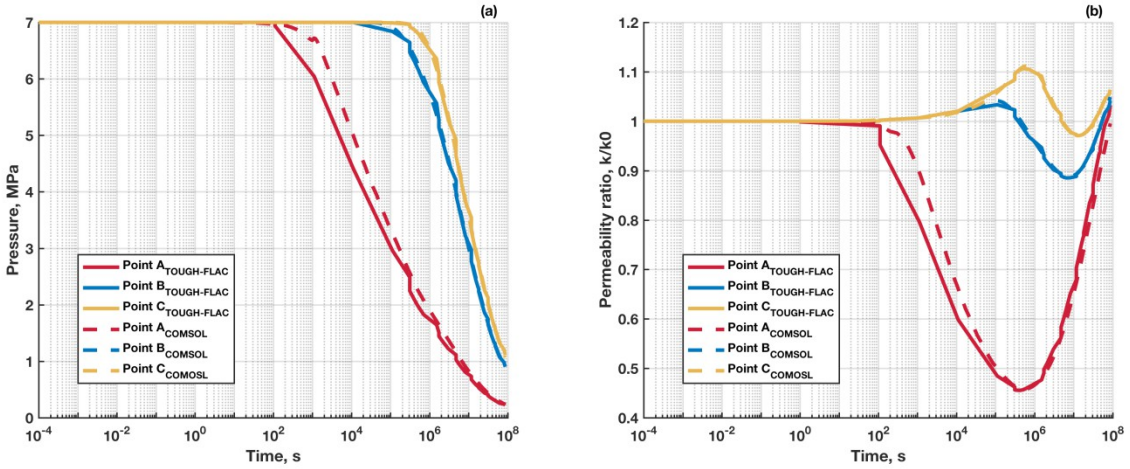

Fig. 5 The evolution of the pore pressure and permeability ratio at Points A, B and C in TOUGH-FLAC and COMSOL for the coupled model with stress-dependent permeability

These results show that the pore pressure at the three points decreases as CH_4 is extracted from the model domain. The effective stress increases due to depressurization, which reduces the permeability to factor of approximately 0.45 the initial value. Due to the relatively low pressure, the predominant factor shifts from the pore pressure to shrinking-induced strain, which increases the permeability in the later stage of production. Generally, the curves produced by TOUGH2 and TOUGH-FLAC exhibit good agreement with those produced by COMSOL. The small difference between them such as at early time in Point A closest to the production boundary may be associated with different boundary pressure settings and different values of the viscosity and density of CO_2.

5 Modeling CO_2-ECBM coupled THM processes with TOUGH-FLAC

The modeling domain and material properties for CO_2-ECBM are given in Fig. 6 and Table 3 (Law et al., 2002; Webb, 2011), respectively. The coal seam is located at a depth of 500 m underground. The reservoir is 5 m in height and has a horizontal production area of 400 m ×

400 m in each grid quarter of the model domain. The initial conditions for the coal seam include a pore pressure of 4 MPa and a temperature of 30 ℃. CO_2 is injected from one corner of model at a constant rate of 0.12 kg/s and at 40 ℃, which is warmer than the initial reservoir temperature. The production wells are placed diagonally to the injection well. The wellbore pressure and temperature are set to 0.1 MPa and 15 ℃, respectively. The other boundaries are no flow boundaries. A constant stress of 11.3 MPa is applied to the top boundary. This stress corresponds to an overburden density of approximately 2260 kg/m^3 and results in an initial vertical stress of 11.3 MPa as well, whereas the horizontal stress is assumed to be 70% of the vertical, at 7.9 MPa. All other boundaries are roller boundaries. The swelling properties for CO_2, CH_4 and N_2 are provided in Table 3. Additionally, the properties of CO_2, N_2 and CH_4 are included in TOUGH2 through the equation-of-state module EOS7C-ECBM; thus, TOUGH-FLAC has the capacity to evaluate more complex cases, such as mixed CO_2 and N_2 injection.

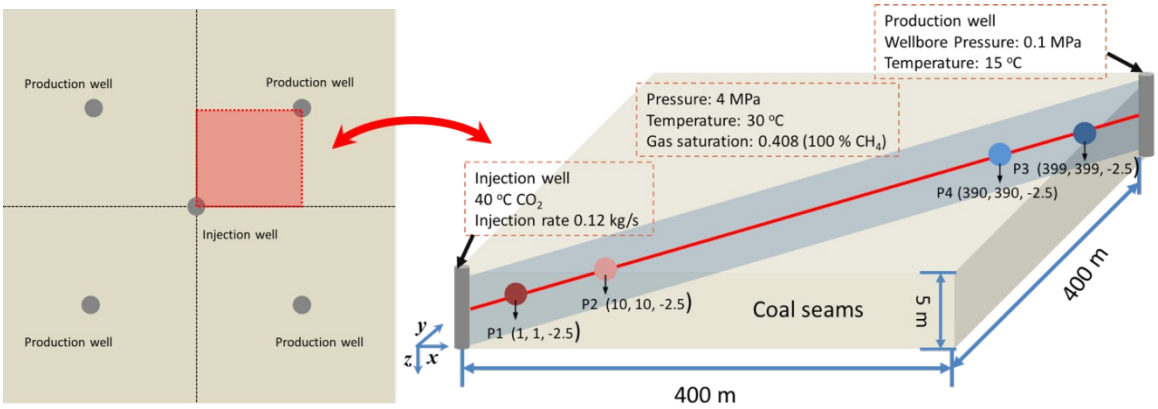

Fig. 6 Description of the geometrical model for ECBM

Fig. 7 shows horizontal and vertical views of the simulation grid used in TOUGH2. The grid is plotted in TOUGH2 based on nodes, which are located at the center of each element. Additionally, grid refinement was applied in the areas near the injection and production wells.

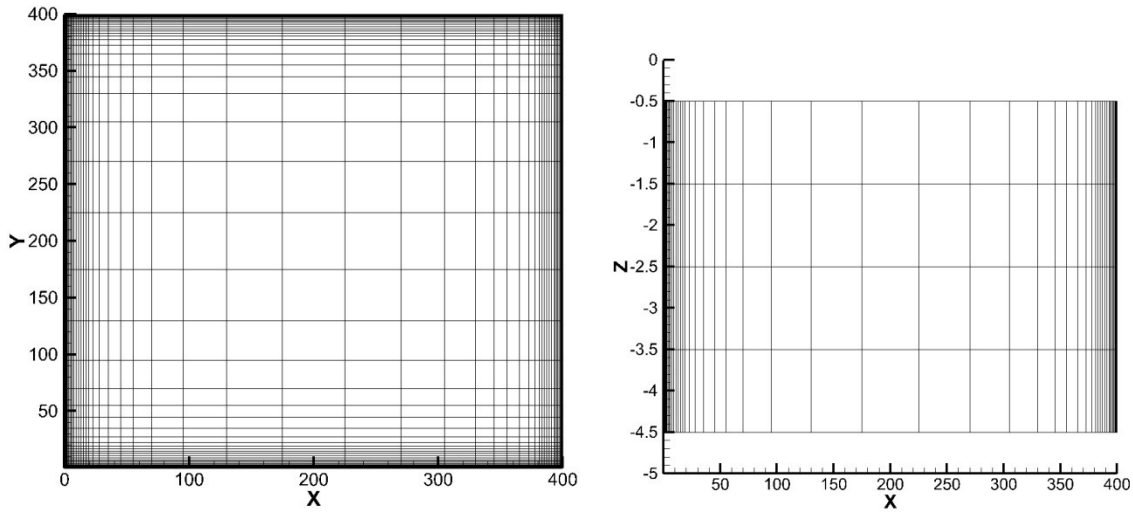

Fig. 7 Grid used in the TOUGH model in the horizontal (left) plane and vertical (right) cross-section

Table 3 Parameters for CO_2-ECBM recovery

	Parameters	Value
Coal	Thickness (m)	5
	Initial porosity, ϕ_0 (%)	2.7
	Initial permeability, k_0 (m^2)	1.0×10^{-14}
	Gas diffusion coefficient (m^2/s)	1.0×10^{-5}
	Liquid diffusion coefficient (m^2/s)	1.0×10^{-10}
	Young's modulus, E (GPa)	3.5
	Poisson's ratio, v	0.25
	Density of coal seam, ρ_c (kg/m^3)	1300
	Moisture content	0.0672
	Ash content	0.156
	Heat conductivity (W/m $℃$)	2.51
	Coal grain specific heat (J/kg $℃$)	920
	Linear thermal expansion coefficient ($1/℃$ ¿)	3.3×10^{-5}
	Capillary pressure model	Eqs. (8) and (9)
	m	0.457
	S_{lr}	0.0
	$1/p_0$ (1/Pa)	5.105×10^{-4}
	P_{max} (Pa)	1×10^{7}
	S_{ls}	1.0
	Relative permeability model	Fig. 1
CH_4	Langmuir pressure constant, p_{LCH_4} (kPa)	4688.5
	Langmuir volume constant, V_{LCH_4} (m^3/kg)	0.0152
	Langmuir volumetric strain, ε_{LCH_4}	0.006
CO_2	Langmuir pressure constant, p_{LCO_2} (kPa)	1903
	Langmuir volume constant, V_{LCO_2} (m^3/kg)	0.0310
	Langmuir volumetric strain, ε_{LCO_2}	0.012
N_2	Langmuir pressure constant, p_{LN2} (kPa)	27241
	Langmuir volume constant, V_{ln2} (m^3/kg)	0.0150
	Langmuir volumetric strain, ε_{ln2}	0.003

5.1 Isothermal case with different permeability models

This section compares the permeability variation based on different stress-dependent permeability models embedded in TOUGH-FLAC. Because the P&M, C&B, and S&D models do not consider the effects of temperature, simulations are conducted under isothermal conditions. Fig. 8 illustrates the temporal evolution of permeability near the injection and production well regions, respectively. Fig. 9 shows the temporal evolutions of pressure P, gas saturation of CO_2 ($S_g^{CO_2}$) and CH_4 ($S_g^{CH_4}$). $S_g^{CO_2}$ and $S_g^{CH_4}$ are calculated by $X_g^{CO_2}S_g$ and $X_g^{CH_4}S_g$, respectively, where $X_g^{CO_2}$ and $X_g^{CH_4}$ represent the mass fraction of gas-phase CO_2 and CH_4. The permeability curves of the four models display similar variation trends. The permeability near the injection well increases slightly until about 2×10^4 s due to rapid strain propagation or displacement in the poro-elastic media (Ma et al., 2016). Then, the permeability decreases significantly due to matrix swelling and then, after 5×10^4 s, increases due to increasing pore pressure (Fig. 9(a)). Near the production well, the permeability decreases as the effective stress increases with the production-induced pressure decline (Fig. 9(b)). Then, after about 1×10^7 s, the permeability decrease stabilizes and even begins to increase slightly due to the low pressure associated with a large shrinkage-strain change in the cleats. The results indicate that the M&R, P&M, and C&B models produce similar permeability evolution. However, the S&D model predicts notably different values of permeability compared to those of the other models because of its different controlling permeability. In the S&D model, permeability is related to horizontal effective stress, whereas in other models permeability is related to mean effective stress.

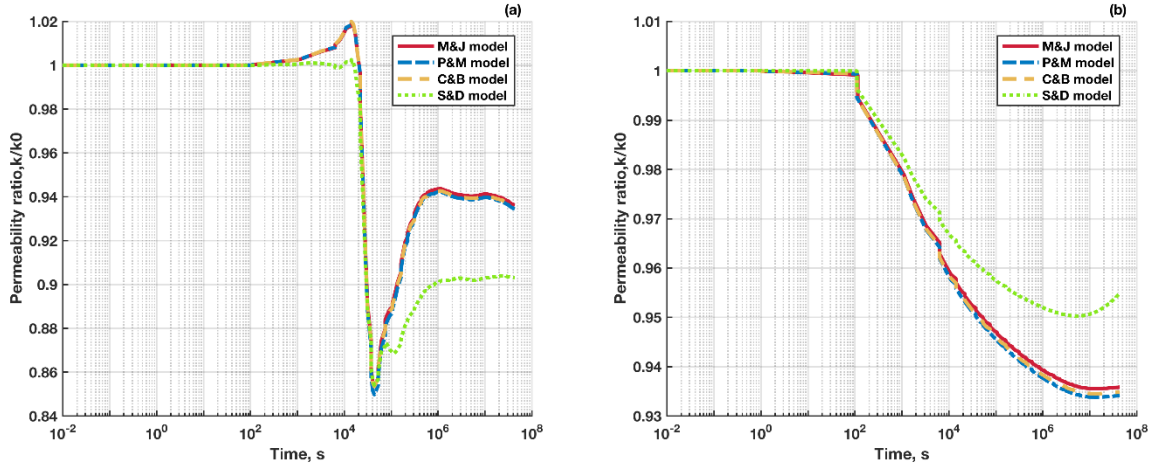

Fig. 8 The evolution of permeability for the isothermal case at Points (a) P1 and (b) P3, which are located near the injection and production wells, respectively

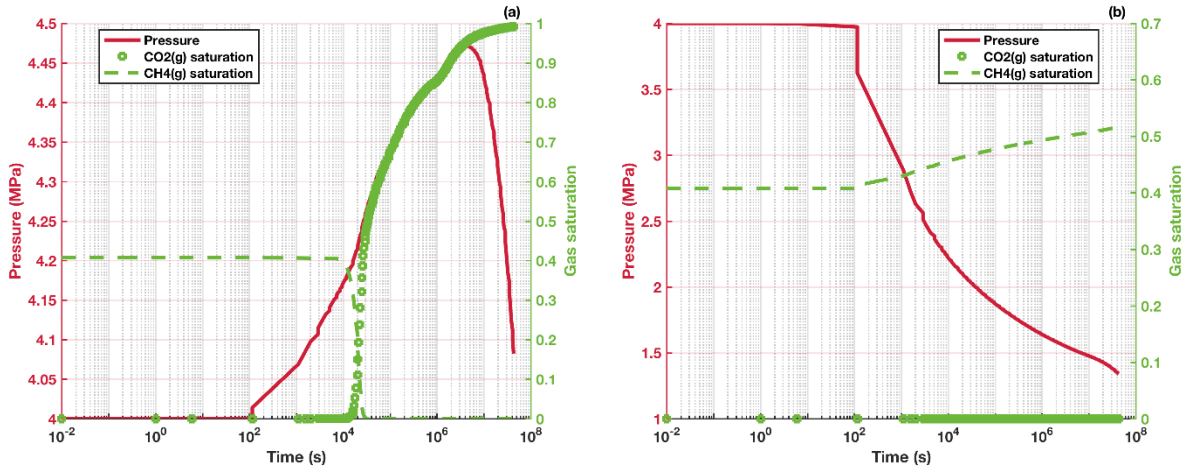

Fig. 9 The evolution of pressure (red lines), CO_2 and CH_4 gas saturation for the for the isothermal case with M&R model at Points (a) P1 and (b) P3, which are located near the injection and production wells, respectively

5.2 Non-isothermal case for CO_2-ECBM recovery

The coupled THM model of CO_2-ECBM recovery is investigated in this section. Fig. 10 presents the spatial distributions of (a) pore pressure P, (b) temperature T, (c) liquid saturation S_l, and (d) the mass fraction of gas-phase $X_g^{CO_2}$ after 1000 days (8.64×10^8 s) of CO_2 injection and production. The pore pressure and temperature increase and decrease near the injection and production areas. With continued injection, CO_2 penetrates into the coal and displaces the water and CH_4.

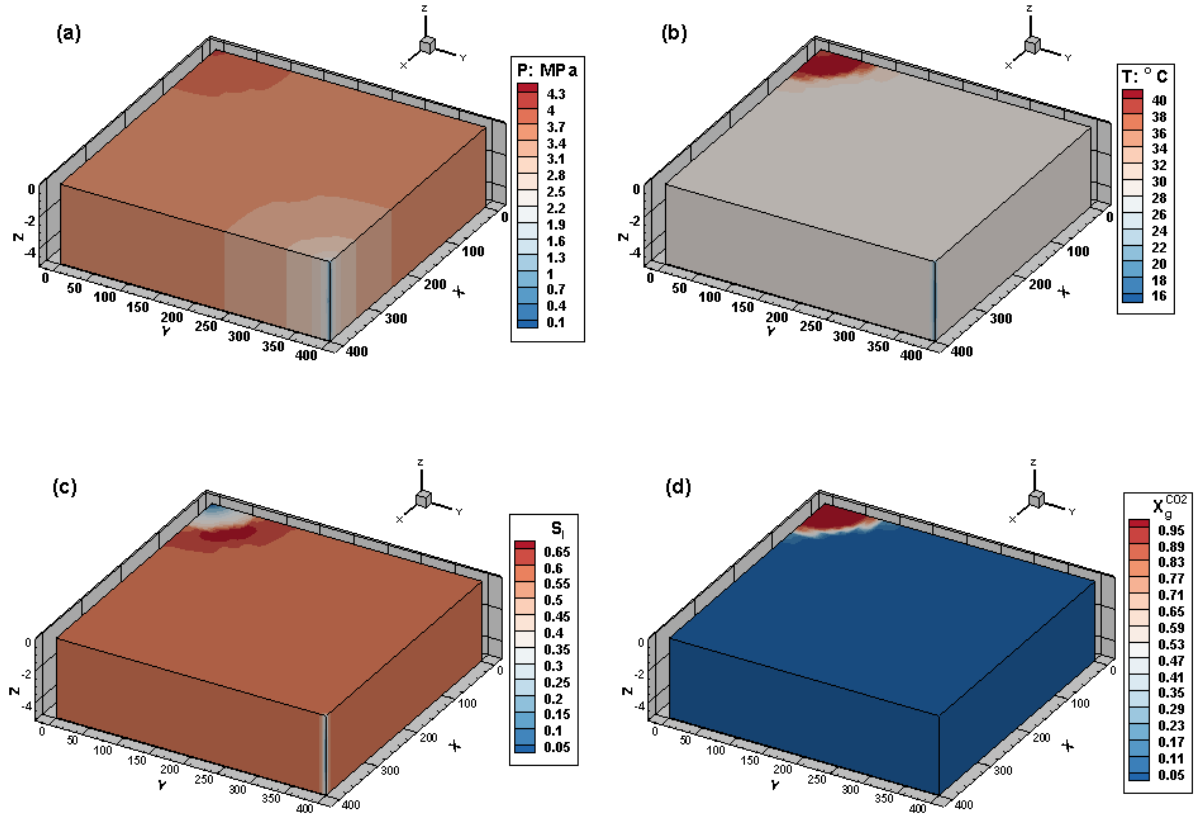

Fig. 10 Spatial distributions of (a) pore pressure P , (b) temperature T , (c) liquid saturation S_L , and (d) the CO_2 mass fraction in gas-phase $X_g^{CO_2}$ after 1000 days of CO_2 injection and CH_4 production

The evolution of pore pressure, temperature, gas saturation, and vertical displacement at P1, P2, P3, and P4 are shown in Fig. 11(a)-(d). The solid lines represent the variations in the four parameters at P1 and P2 near the injection well, while the dashed lines are the curves at P3 and P4 close to the production well. As CH_4 and water are extracted from the production well, the pore pressure generally decreases and results in coal subsidence. Due to the low temperature and liquid saturation values at the production wellbore, the temperature and saturation considerably decrease over time.

The pore pressure at P1 exhibits a small increase after approximately 100 s as affected by the nearby CO_2 injection. At this early time of 100 s, temperature, saturation, and displacement exhibit minor changes. With continued CO_2 injection into the reservoir, the advective CO_2 approaches P1and P2 and increases the pressure, temperature, and displacement. Because CO_2 is approximately 20 times more soluble in water than is CH_4, the gas saturation first decreases and then increases with CO_2 injection. At thermodynamic equilibrium, the increasing pore pressure leads to a temperature peak of approximately 42 $℃$ and then decreases. In the later stage, the area of influence associated with production reaches P1 and P2 and decreases the pore pressure. After approximately 5×10^5 s (approximately 5.79 days), the vertical displacement

substantially decreases due to the reduction of swelling effects and decreases in the pore pressure and temperature.

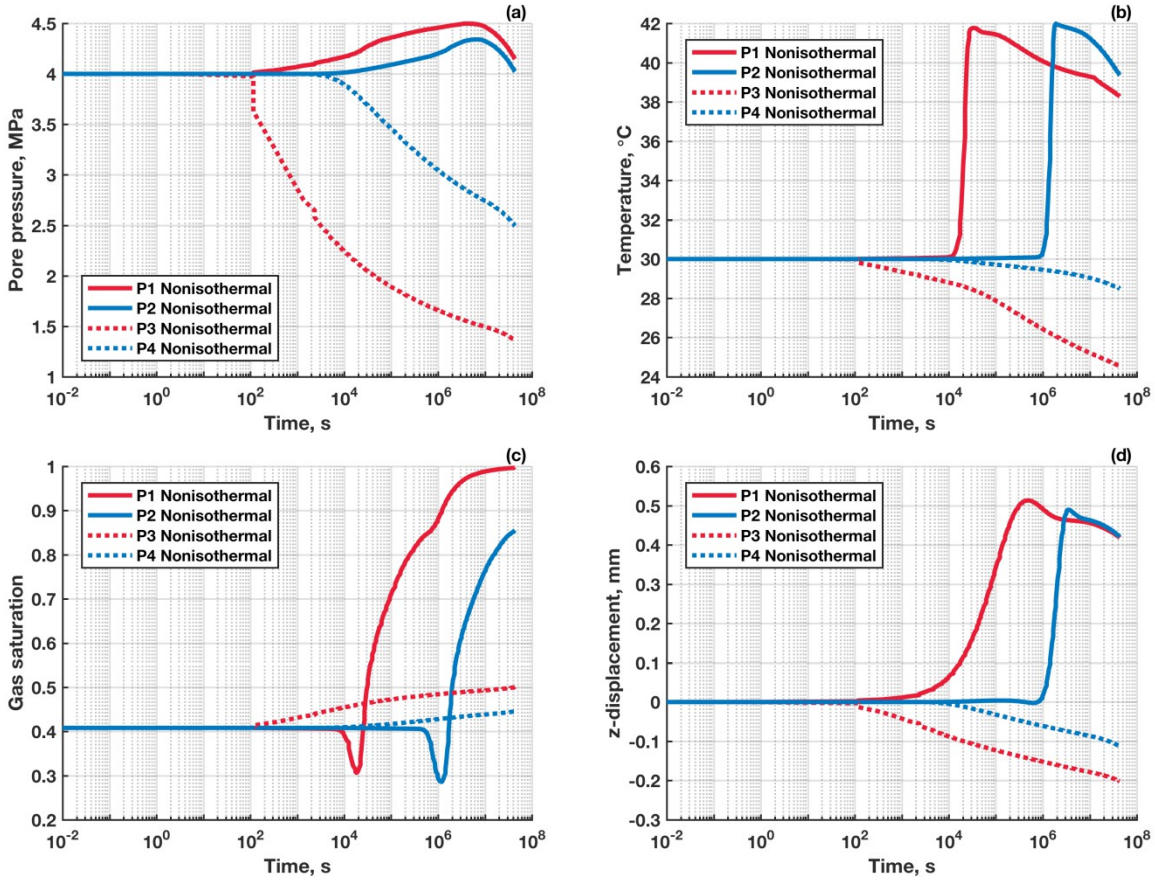

Fig. 11 The evolution of (a) pore pressure, (b) temperature, (c) total gas saturation and (d) vertical displacement at P1, P2, P3, and P4

The swelling strain changes due to CO_2 and CH_4 are presented in Fig. 12. Assuming a fully constrained boundary, the maximum possible stress that could be induced by thermal expansion is near the injection well is approximately 2.7 MPa, which corresponds to a linear thermal expansion coefficient of 3.3 $\times$ 10^{-5} $℃^{-1}$ temperature change of approximately 12 $℃$ and coal bulk modulus of 2.3333 GPa . The negative swelling change suggests that the matrix is shrinking. The total volumetric strain change associated with swelling, as defined in Eq. (15), is approximately 4.4 $\times$ 10^{-3}, which is also correspond to the sum of swelling strain for CO_2 and CH_4 in Figure 12. A swelling strain of 4.4 $\times$ 10^{-3} could results in stress change of as high as approximately 10 MPa assuming fully constrained conditions. Thus, the thermal stress and the swelling stress could both be important and in this case the latter has more significance.

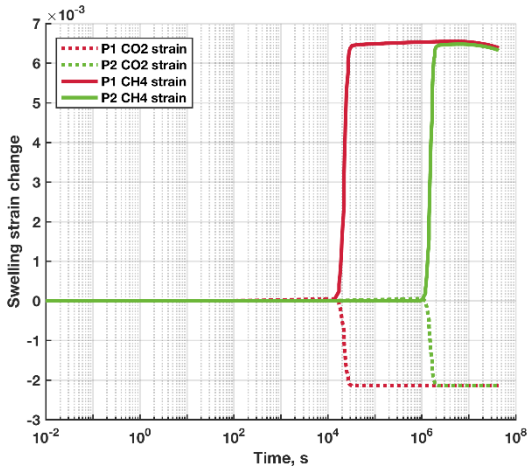

Fig. 12 The variations in swelling stress change caused by CO_2 adsorption and CH_4 desorption at P1 and P2

The mean total and effective stresses are shown in Fig. 13. For the non-isothermal case, the total stress changes are associated with three contributions: (1) pore pressure, (2) swelling/shrinkage strain from CO_2 adsorption or CH_4 desorption, and (3) thermal stress. The stresses at P1 and P2 exhibit similar variations (Fig. 13(a)). The total compressive stress first decreases slightly as a result of the pore pressure increase, but it then increases dramatically and peaks at approximately -13.8 MPa as a consequence of the swelling effects caused by CO_2 adsorption onto the coal matrix and thermal expansion. Fig. 13(b) shows the stress changes at P3 and P4. With CH_4 depletion, the effective stress increases due to the governing influence of depressurization, However, the total stress decreases mainly as a result of coal matrix shrinkage and decreased temperature.

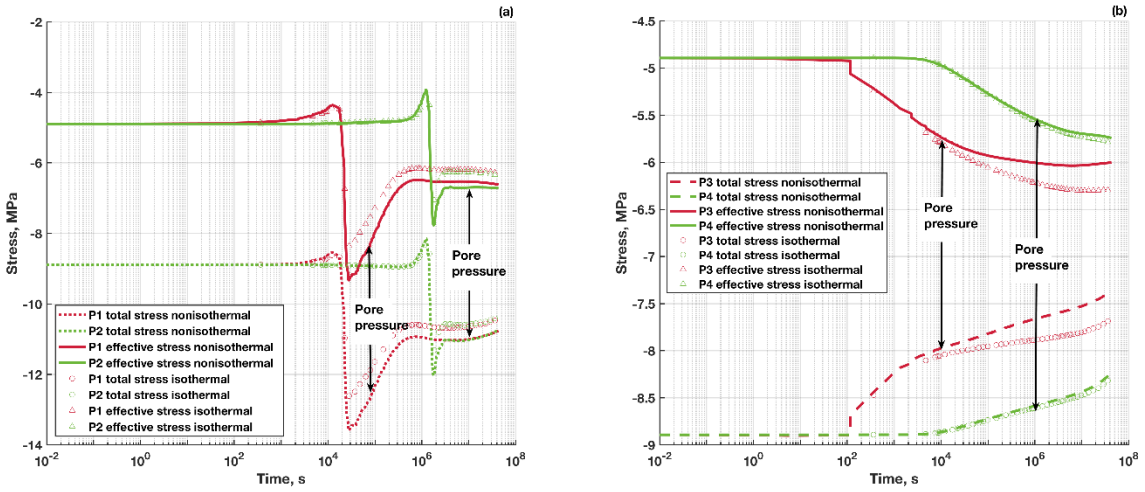

Fig. 13 Temporal evolution of the total and effective mean stresses at (a) P1 and P2 and (b) P3 and P4 for non-isothermal (lines) and isothermal (markers) cases

Fig. 14 presents the evolution of the horizontal and vertical effective stresses at P1 and P2 (a) and P3 and P4 (b). The differences between stress variations in the horizontal and vertical

directions are associated with the different mechanical boundary conditions. Due to constant stress loading at the top boundary, the vertical stress at P1 and P2 that is mainly induced by swelling reduces after adsorption equilibrium is reached; the changes of vertical stress at P3 and P4 are proportional to changes in fluid pressure. However, swelling and thermal effects influence the horizontal stress due to the zero displacement constraint. The stresses caused by swelling and thermal effects are zero for the element with free boundary, but they contribute to 100% of the total stress change for a full displacement constraint. These results show that horizontal stresses are strongly affected by thermal expansion and adsorption swelling (P1 and P2) and decreased pressure (P3 and P4). Fig. 13(a) and 14(a) show that the influences of swelling and thermal effects decrease as the distance from the injection well increases.

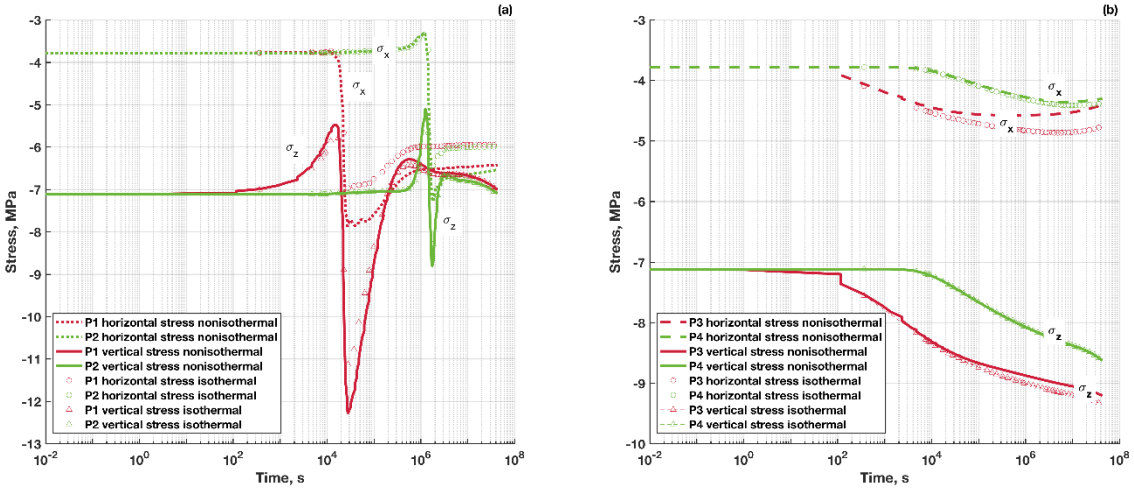

Fig. 14 Temporal evolution of the horizontal and vertical effective stresses at (a) P1 and P2 and (b) P3 and P4

The effective stress paths at P1 and P3 are presented in Fig. 15(a) and (b), respectively. The yield surface satisfies the Mohr-Coulomb criterion as follows:

$$\sigma_1^{'}=\frac{2C^{'}cos(\phi)}{1-\sin(\phi)}+\frac{1+\sin(\phi)}{1-\sin(\phi)}\sigma_3^{'} \quad (19)$$

where $\sigma_1^{'}$ and $\sigma_3^{'}$ are the maximum and minimum principle effective stress, respectively. $C^{'}$ is the cohesion, which is assumed to equal zero. ϕ is the frictional angle of coal, which ranges from $30°$ to $67.8°$ (Gu, F., 2006). In our model, ϕ is set to 30□. Thus, mechanical failure occurs if $\sigma_1^{'}\geq 3\sigma_3^{'}$. Three cases with the different stress ratios of σ_h/σ_v (where σ_h is the horizontal stress and σ_v is the vertical stress) are investigated. These cases represent three different types of *in situ* stress states: (1) extensional, (2) isotropic, and (3) compressional regimes. The principal effective stress at P3 continues to increase due to gas depletion. In the process of CBM depletion, the stress never reaches the yield surface; thus, no failure occurs. With sustained CO_2 injection, the stress at P1 in the isotropic and compressional regimes does not approach the yield surface. In the extensional regime, the effective principal stress moves rapidly toward the yield surface due to the significant shear stress caused by the different mechanical constraints in the different directions. After 20275 s (0.234 days), the stress

path moves away from the failure area due to increases in the maximum and minimum stresses, both of which are affected by swelling and thermal expansion. The *in situ* stress state has a considerable influence on the potential mechanical failure. The simulation results indicate that failure is more likely to occur at a site with an extensional initial stress regime. Specific attention should be given to such conditions during the early production time.

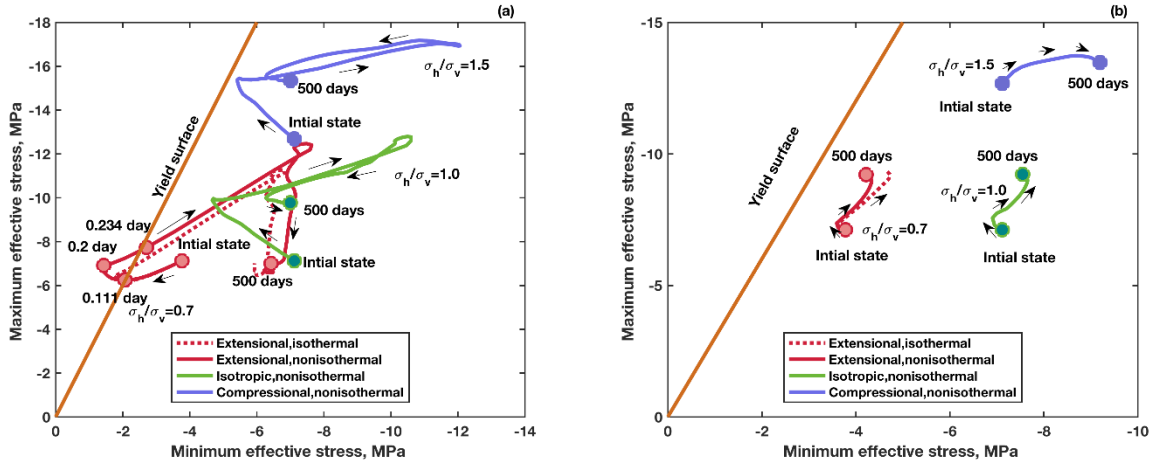

Fig. 15 Effective stress paths at (a) P1 and (b) P3 for stress ratios of 0.7, 1.0 and 1.5. The stress for an isothermal case with a ratio of 0.7 is represented by the red dashed lines.

6 Summary and conclusions

In this paper, coupled, multiphase and multicomponent hydraulic, thermal, and geomechanical (THM) behavior are investigated during CO_2-ECBM recovery. The coupled simulator TOUGH-FLAC is applied to simulate CO_2-ECBM for the first time. During the THM simulation, gas migration and adsorption, liquid flows and heat transfer are calculated in TOUGH2. The deformation associated with pore pressure change, thermal expansion and swelling is calculated in FLAC3D using a quasi-static approach. To assess the feasibility and accuracy of TOUGH2 and TOUGH-FLAC, a comparison is made between the simulator and COMSOL Multiphysics software, and the simulation results exhibited a good agreement. This provides code-to-code verifications of the software involved.

Then, a 3D model is established to study the hydromechanical responses during CO_2-ECBM recovery. One of the key factors in CO_2-ECBM recovery is the absolute permeability. The variation in the coal permeability is sensitive to the effective stress, the swelling or shrinkage strain associated with CO_2 adsorption or CH_4 desorption as well as thermal expansion. An isothermal case is first simulated to analyze the changes in permeability using four stress-dependent permeability models in the simulators. The four permeability models predict similar evolution in permeability during the production. However, there is a notable difference between the S&D results and those of the other models due to the different controlling factors, such as the horizontal versus mean effective stress.

Next, a non-isothermal case is studied. As CH_4 and water are extracted from the coal seam, the pore pressure, temperature, liquid saturation and vertical displacement continually decrease. The decreased pore pressure increases the effective stress in the vertical and horizontal directions, as

well as the corresponding mean stress. This increase in the mean stress tends to prevent failure in the coal seam. Injecting warm CO_2 into the coal changes the hydromechanical behavior inside the coal seam. A significant shear stress is observed as a result of the boundary constraints in different directions, which could cause the stress path to reach the yield surface in the case of an extensional stress regime. Later, CO_2 adsorption matrix induced matrix swelling and thermal expansion tends to prevent failure in the coal seam.

In this study, an isotropic single coal seam is considered, but the inner pore and fracture structures suggest that coal has anisotropic properties, especially highly fractured coal. The permeability of fractures in each direction is affected by the stress normal to the fractures and not the mean effective stress. Therefore, anisotropic permeability will be proposed in future research.

Acknowledgments

This study was supported by Special Subject Grant of National “973” Basic Research Program of China (No. 2015CB251602 and No.2009CB219605), National Natural Science Foundation of China (No. 41074040 and No. 50774083), Jiangsu Natural Science Foundation (No. BK20141125), Chinese Program for New Century Excellent Talents in University (No. NCET-07-0803) and Opening Fund (NO. 2016A01). The work was funded in part by the U.S. Department of Energy under contract no. DE-AC02-05CH11231. Special thanks to the anonymous reviewers for their valuable comments.

References

Benson, S.M., Cole, D.R., 2008. CO2 Sequestration in deep sedimentary formations. Elements 4, 325–331.

Connell, L.D., 2009. Coupled flow and geomechanical processes during gas production from coal seams. Int. J. Coal Geol. 79, 18–28.

Connell, L.D., Detournay, C., 2009. Coupled flow and geomechanical processes during enhanced coal seam methane recovery through CO_2 sequestration. Int. J. Coal Geol., CO_2 Sequestration in Coals and Enhanced Coalbed Methane Recovery 77, 222–233.

Cui, X., Bustin, R.M., 2005. Volumetric strain associated with methane desorption and its impact on coalbed gas production from deep coal seams. AAPG Bull. 89, 1181–1202.

Cui, X., Bustin, R.M., Dipple, G., 2004. Differential transport of CO2 and CH4 in coalbed aquifers: implications for coalbed gas distribution and composition. AAPG Bull. 88, 1149–1161.

Gray, I., 1987. Reservoir engineering in coal seams: part 1-the physical process of gas storage and movement in coal seams. SPE Reserv. Eng. 2, 28–34.

Gu, F., Chalaturnyk, R., 2010. Permeability and porosity models considering anisotropy and discontinuity of coalbeds and application in coupled simulation. J. Pet. Sci. Eng. 74, 113–131.

Gu, F., Chalaturnyk, R.J., 2005. Sensitivity study of coalbed methane production with reservoir and geomechanic coupling simulation. J. Can. Pet. Technol. 44, PETSOC-05-10-02. http://dx.doi.org/10.2118/05-10-02.

Gu, F., Chalaturnyk, R.J., 2006. Numerical simulation of stress and strain due to gas sorption/desorption and their effects on in situ permeability of coalbeds. J. Can. Pet. Technol. 45, PETSOC-06-10-05. http://dx.doi.org/10.2118/06-10-05.

Itasca, http://www.itascacg.com/(accessed 7.23.16).

Jeanne, P., Rutqvist, J., Vasco, D., Garcia, J., Dobson, P.F., Walters, M., Hartline, C., Borgia, A., 2014. A 3D hydrogeological and geomechanical model of an enhanced geothermal system at the geysers, California. Geothermics 51, 240–252.

Kashihara, K., Rutqvist, J., 2016. Temperature-dependent deformation prediction of oil sand by coupled geomechanical and fluid flow modeling, in: SPE Canada Heavy Oil Technical Conference, 7-9 June 2016, Calgary, Alberta, Canada.

Law, D.H.S., Meer, V.D.L.G.H., Gunter, W.D., 2002. Numerical simulator comparison study for enhanced coalbed methane recovery processes, Part I: pure carbon dioxide injection, in: SPE Gas Technology Symposium, 30 April-2 May 2002, Calgary, Alberta, Canada.

Law, D.H.S., Meer, V.D.L.G.H.B., Gunter, W.D.B., 2004. Comparison of numerical simulators for greenhouse gas sequestration in coalbeds, part III: more complex problems - 128.pdf. Presented at the the 7th International Conference on Greenhouse Gas Control Technologies, Vancouver BC, Canada.

Liu, H.H., Rutqvist, J., 2009. A new coal-permeability model: internal swelling stress and fracture-matrix interaction. Transp. Porous Media 82, 157–171.

Liu, J., Chen, Z., Elsworth, D., Qu, H., Chen, D., 2011. Interactions of multiple processes during CBM extraction: a critical review. Int. J. Coal Geol. 87, 175–189.

Ma, T., Rutqvist, J., Weiqun, L., Zhu, L., Kunhwi, K., 2016. Modeling of CO2 sequestration in coal seams: role of CO2-induced coal softening on injectivity, storage efficiency and caprock deformation.

Moore, R., Palmer, I., Higgs, N., 2014. Anisotropic model for permeability change in coalbed-methane wells. Society of Petroleum Engineers 18, 456–462.
Moore, T.A., 2012. Coalbed methane: a review. Int. J. Coal Geol. 101, 36–81.
Oldenburg, C.M., Moridis, G.J., Spycher, N. and Pruess, K., 2004. EOS7C version 1.0: TOUGH2 module for carbon dioxide or nitrogen in natural gas (methane) reservoirs. Lawrence Berkeley National Laboratory.
Palmer, I., 2009. Permeability changes in coal: analytical modeling. Int. J. Coal Geol., CO2 Sequestration in Coals and Enhanced Coalbed Methane Recovery 77, 119–126.
Palmer, I., Mansoori, J., 1998. How permeability depends on stress and pore pressure in coalbeds: a new model. SPE Reserv. Eval. Eng. 1, 539–544.
Pan, Z., Connell, L.D., 2011. Impact of coal seam as interlayer on CO2 storage in saline aquifers: a reservoir simulation study. Int. J. Greenhouse Gas Control 5, 99–114.
Pan, Z., Connell, L.D., 2012. Modelling permeability for coal reservoirs: a review of analytical models and testing data. Int. J. Coal Geol. 92, 1–44.
Pruess, K., Oldenburg, C.M., Moridis, G.J., 2012. TOUGH2 user's guide version 2, Lawrence Berkeley Natl. Lab., Berkeley.
Roadifer, R.D., Moore, T.R., Raterman, K.T., Farnan, R.A., Crabtree, B.J., 2003. Coalbed methane parametric study: what’s really important to production and when?, Society of Petroleum Engerines.
Robertson, E.P., Christiansen, R.L., 2006. A permeability model for coal and other fractured, sorptive-elastic media, in: SPE Eastern Regional Meeting, 11–13 October 2006, Canton, Ohio, USA.
Rutqvist, J., 2011. Status of the TOUGH-FLAC simulator and recent applications related to coupled fluid flow and crustal deformations. Comput. Geosci. 37, 739–750.
Rutqvist, J., Chijimatsu, M., Jing, L., Millard, A., Nguyen, T.S., Rejeb, A., Sugita, Y., Tsang, C.F., 2005. A numerical study of THM effects on the near-field safety of a hypothetical nuclear waste repository-BMT1 of the DECOVALEX III project. Part 3: effects of THM coupling in sparsely fractured rocks. Int. J. Rock Mech. Min. Sci. 42, 745–755.
Rutqvist, J., Moridis, G.J., Grover, T., Silpngarmlert, S., Collett, T.S., Holdich, S.A., 2012. Coupled multiphase fluid flow and wellbore stability analysis associated with gas production from oceanic hydrate-bearing sediments. J. Pet. Sci. Eng. 92-93, 65–81.
Rutqvist, J., Tsang, C.-F., 2002. A study of caprock hydromechanical changes associated with CO2-injection into a brine formation. Environ. Geol. 42, 296–305.
Seidle, J.P., Jeansonne, M.W., Erickson, D.J., 1992. Application of matchstick geometry to stress dependent permeability in coals, in: SPE Rocky Mountain Regional Meeting, 18-21 May 1992, Casper, Wyoming.
Shi, J.Q., Durucan, S., 2004. Drawdown induced changes in permeability of coalbeds: a new interpretation of the reservoir response to primary recovery. Transp. Porous Media 56, 1–16.
Wang, G.X., Massarotto, P., Rudolph, V., 2009. An improved permeability model of coal for coalbed methane recovery and CO2 geosequestration. Int. J. Coal Geol. 77, 127–136.
Webb, S.W., 2011. EOS7C-ECBM Version 1.0, Additions for Enhanced Coal Bed Methane Including the Dusty Gas Model, Sandia Park, NM.
White, C.M., Smith, D.H., Jones, K.L., Goodman, A.L., Jikich, S.A., LaCount, R.B., DuBose, S.B., Ozdemir, E., Morsi, B.I., Schroeder, K.T., 2005. Sequestration of carbon dioxide in coal with enhanced coalbed methane recoverya review. Energy and Fuels 19, 659–724.